An asymmetric pinching damaged hysteresis model for glubam members: Parameter identification and model comparison

(Article begins on next page)

21 April 2025

Computers and Structures

An asymmetric pinching damaged hysteresis model for glubam members: parameter identification and model comparison
--Manuscript Draft--

Abstract:	Abstract The performance of glue laminated bamboo (glubam) members is governed by the nonlinear response at their joints, where high deformation levels and stress concentrations are developed. Numerous phenomenological models are presently employed to describe the hysteresis behavior of these joints, while these models always have an excessive number of parameters, and the physical interpretation of these parameters is often challenging. Moreover, some hysteresis models cannot capture all hysteresis features such as asymmetry, pinching, and damage. Consequently, this paper introduces a novel phenomenological-based hysteretic model named Asymmetric Pinching Damaged (APD) model, and implemented it in Abaqus by combining connector and spring elements in series or parallel. This model encompasses asymmetry, pinching, and strength degradation for bamboo joint components, with parameters that possess clear physical meanings and are readily comprehensible. This study also presented a parameter identification framework coupling the Parallel Genetic Algorithm (PGA) and Bayesian Neural Network (BNN). By merging the FE modeling and optimizing algorithms with the interactive application of ABAQUS and Python software platforms, the integrated identification framework is capable of performing multi-threaded parallel computation of finite element models considering the BNN-based uncertainty quantification, thus greatly improving the efficiency of parameter identification.

Highlights

- Asymmetric pinching damaged hysteresis model for glue laminated bamboo (glubam) members
- Parameters identification coupling Bayesian Neural Network (BNN) and PGA
- Comprehensive validation and comparison against other hysteretic models

Dear Editors,

On behalf of my co-authors, we thank you very much for giving us the opportunity to revise our manuscript. We thank the Editor and the Reviewers for their comments and suggestions concerning our manuscript (Ref. No.: CAS-D-24-00504). The authors would like to thank the Reviewers for the extremely careful reading of the manuscript and for providing us with comments and suggestions to improve its quality.

The following responses have been prepared to address the Reviewers' technical comments in a point-by-point fashion. The list of questions raised follows, together with our response to each (in blue).

We tried our best to improve the manuscript, by also making some additional changes to clarify some of the concerns raised. We think that the manuscript has been greatly improved by these revisions and we hope that you will now find it suitable for publication in Computers and Structures.

Once again, thank you very much for your comments and suggestions!

On behalf of the authors,

Cristoforo Demartino, Ph.D., P.E.,

Department of Architecture, Roma Tre University, Rome, Italy
Email: cristoforo.demartino@me.com

An asymmetric pinching damaged hysteresis model for glubam members: parameter identification and model comparison

Da Shi[a,b], Cristoforo Demartino[c,*], Giuseppe Carlo Marano[b], Yongjia Xu[d]

[a] *College of Civil Engineering and Architecture, Zhejiang University, 866 Yuhangtang Road, Hangzhou, 310058 Zhejiang, PR China*

[b] *Politecnico di Torino, DISEG, Dipartimento di Ingegneria Strutturale, Edile e Geotecnica, Corso Duca Degli Abruzzi, 24, Turin, 10128, Italy*

[c] *Department of Architecture, Roma Tre University, Rome, 00153, Italy*

[d] *Zhejiang University - University of Illinois Urbana Champaign Institute, Haining 314400, Zhejiang, PR China*

Abstract

The performance of glue laminated bamboo (glubam) members is governed by the nonlinear response at their joints, where high deformation levels and stress concentrations are developed. Numerous phenomenological models are presently employed to describe the hysteresis behavior of these joints, while these models always have an excessive number of parameters, and the physical interpretation of these parameters is often challenging. Moreover, some hysteresis models cannot capture all hysteresis features such as asymmetry, pinching, and damage. Consequently, this paper introduces a novel phenomenological-based hysteretic model named Asymmetric Pinching Damaged (APD) model, and implemented it in Abaqus by combining connector and spring elements in series or parallel. This model encompasses asymmetry, pinching, and strength degradation for bamboo joint components, with parameters that possess clear physical meanings and are readily comprehensible. This study also presented a parameter identification framework coupling the Parallel Genetic Algorithm (PGA) and Bayesian Neural Network (BNN). By merging the FE modeling and optimizing algorithms with the interactive application of ABAQUS and Python software platforms, the integrated identification framework is capable of performing multi-threaded parallel computation of finite element models considering the BNN-based uncertainty quantification, thus greatly improving the efficiency of parameter identification.

Keywords: , Glue laminated bamboo, Asymmetric Pinching Damaged (APD) hysteretic models, Parameter identification, Parallel genetic algorithm, Bayesian neural network

*Corresponding author: Cristoforo Demartino, cristoforodemartino@intl.zju.edu.cn

Email addresses: da.21@intl.zju.edu.cn (Da Shi), cristoforo.demartino@me.com (Cristoforo Demartino), giuseppe.marano@polit.it (Giuseppe Carlo Marano), xuyongjia0904@163.com (Yongjia Xu)

1. Introduction

Structural bamboo is a renewable resource abundantly accessible, exhibiting a lower environmental footprint compared to other construction materials of similar strength. The structural performance of glue laminated bamboo (glubam) constructions is significantly influenced by the nonlinear response observed in the connection zones. These areas, characterized by high levels of deformation and stress concentration, form around fasteners such as nails, dowels, or bolts. Furthermore, these zones are particularly susceptible to significant load reversals throughout the service life of structures, especially under extreme conditions such as earthquakes or strong winds. Therefore, investigating the nonlinear behavior of glubam connections under substantial deformation levels until failure is essential.

The hysteretic behavior of glubam members is governed mainly by the crushing of glubam, the plasticity of fasteners, and friction between components [1, 2, 3]. As a quasi-brittle material, glubam poses a strength/stiffness threshold that irreversibly degrades when surpassed. This degradation leads to a delay in the connection response and drop the stiffness each connector provides [4], reflected in the hysteresis as one of the most recognizable nonlinear features of wood-based structures named as "pinching". Furthermore, various increasingly prevalent circumstances in structural design can cause significant deviations from the classical symmetrical hysteretic behavior of glubam members, resulting in remarkably asymmetrical responses. The main reasons of asymmetry include the lateral-axial load combinations [5], hybrid connections with stiffer and thicker materials [6, 7, 8, 9], and overturning anchorage systems [10, 11, 12]. Therefore, asymmetry should be carefully handled in the response simulation of bio-based materials.

The complexity of wood-based member behavior has motivated the creation of several hysteretic models. Three main groups exist in the literature: (i) detailed micro-models, where each material is represented individually (e.g., steel and wood) with 3D solid and contact finite elements on a mechanical formulation (e.g., plasticity or continuum damage mechanics). Such models can predict accurate nonlinear response of detailed members/assemblies at expenses of extensive computation efforts [13]; (ii) component macro-models, in which each component (e.g., fasteners, anchors, sheathing/mass timber panels, and frame) is modeled separately using a set of nonlinear coupled or uncoupled springs and/or shell elements, generally based on mechanical and/or phenomenological formulations. These models are typically applied to simulate the dynamic response of planar members or assemblies with an efficient accuracy-to-time ratio (e.g., dowel-type joints [14], Light-frame timber (LFT) walls [15, 16, 12], Cross laminated timber (CLT) walls [17, 18, 19, 20, 21], and Cross laminated timber (CLT) slabs [22]); and (iii) simplified macro-models, where the whole member is simulated with a set of uncoupled/coupled uniaxial Single Degree-Of-Freedom (SDOF) nonlinear springs [23, 24, 25, 26], stated on a phenomenological approach and used for a fast dynamic performance evaluation of the entire structure at expenses of neglect coupling load effects [18]. Among all these options, phenomenological models are most versatile in simulating a broad variety of timber assemblies

with symmetric/asymmetric behavior, which is the objective of this article.

There are usually two ways to construct phenomenological hysteresis models. One is to program the constitutive rules through user-subroutines to construct user-defined material properties, and the other is to construct new models based on existing basic constitutive material models using series-parallel rules. For the former method, programming of user-subroutines is needed [27, 28, 29]. However, the programming is complex and may also cause convergence problems. Thus, this paper aims at developing a hysteretic model based on existing basic constitutive material models using series-parallel rules. The proposed model in this work explains the mechanism of asymmetric pinching damaged hysteresis behavior, reflecting the asymmetry, pinching, and strength/stiffness degradation behaviors, while being computationally efficient and suitable for implementation in structural-level finite element (FE) analysis.

To simulate the complex behaviors of glubam joints mentioned above, the proposed model is expected to show a large number of flexible parameters. Hence, automatic parameter calibration is indispensable. Traditional parameter optimization (identification) methods may fall short in solving this highly non-linear and non-convex optimization problem. To improve the practical value of the proposed model, three innovative methods for parameter identification are investigated and compared in this study: (i) Parallel Genetic Algorithms (PGA), (ii) Bayesian Inference (BI) and (iii) coupling method of Bayesian Neural Network (BNN) (Graves [30], Blundell et al. [31]) and PGA (named as BNN-PGA). By scripting programming in Python, the proposed PGA, BI and BNN-PGA method are fully automated to interact with ABAQUS software for carrying out multi-thread parallel finite element analyses during identification process. Parallel computing of FE modeling will serve to make identification faster, and the inference and uncertainty quantification of BNN can further improve the overall optimization efficiency.

In the following sections, Section 2 presented the constitutive equations of the proposed hysteretic model. Section 3 calibrated the APD hysteresis model parameters roughly, and outlined the fundamental procedures of three parameter identification frameworks (PGA, BI and BNN-PGA). The calibrated model after parameter identification was validated and compared against a set of experimental results of glubam components in Section 4, where it was also compared with the response of three other well-known hysteretic models available in the literature (SAWS, Pinching4, and DowelType).

2. APD hysteresis model

The hysteretic behavior of glubam members is governed mainly by the crushing of glubam and the plasticity of fasteners. Both of them contribute to the final hysteretic behavior of the entire member. Therefore, the APD hysteresis model for entire glubam member was developed by coupling the hysteretic behaviors of these two individual components. The model formulation is presented in detail herewith. This model is designed following the series-parallel rule (Levitin et al. [32], Numanoglu et al. [33], Wang et al.

[34]). Series-parallel rules refer to the configuration of components or systems where certain elements are connected in series, while others are connected in parallel. This approach is commonly used in various fields, including electrical engineering, mechanical systems, and structural modeling. In a series connection, components are arranged sequentially so that the same output (e.g., force) flows through each element. In contrast, a parallel connection involves arranging components so that they share the same input (e.g., displacement), but the output is distributed among them.

In this study, series-parallel rules play a crucial role. The overall behavior of a joint can be complex, involving multiple elements that need to interact in specific ways to replicate real-world phenomena like pinching, asymmetry, energy dissipation, stiffness degradation, and strength deterioration. By applying series-parallel rules in hysteretic behavior modeling, a more flexible and resilient joint model, capable of handling various loading conditions, can be developed. This approach is particularly valuable when dealing with materials or structures that exhibit non-linear and path-dependent behaviors, such as those observed in glubam joints or other composite materials. Noting that this model is an improvement version of the model proposed in Xu et al. [35], Shi et al. [36, 37]. The basic materials and some assumptions are similar, but the asymmetry and damage effect are more comprehensively considered in the current model. In addition, the model behavior is further validated based on experimental results. Such improvements allows the model to represent the complex behaviors of bio-based materials better.

2.1. Basic material model

This section will introduce the constitutive rule of basic material model used in APD hysteresis model including elasto-plastic rule (herein EP material model), STOP rule (herein S material model) and LOCK rule (herein L material model). The EP material model requires the specification of four parameters: (i) elastic stiffness, (ii) yield strength, (iii) post-yield stiffness, and (iv) hardening rule. As depicted in Figure A.17, this study employs both isotropic and kinematic hardening rules for the EP material model, named as EP-ISO and EP-KIN, respectively. STOP materials can be visualized as a slider in a slot with fixed boundaries. The deformation is constrained by these boundaries, allowing frictionless relative movement within the slots' limits. When the distance to one end of the slot is finite and the other is effectively infinite, the STOP material acts as a one-sided constraint. Consequently, STOP materials are categorized into Tension-STOP (TS) and Compression-STOP (CS) types, restricted on the tension and compression sides, respectively (shown in Figure A.16). As illustrated in Figure A.18, the LOCK material model operates based on a threshold value defined by either deformation or internal force. The material behaves according to its initial properties until this threshold is met. Once the threshold is reached, the material becomes "locked" and behaves as a rigid body. In this study, the LOCK material is characterized by linear-elastic behavior with the threshold defined by internal force. For further details on the EP, STOP and LOCK material models, see Shi et al. [36, 37].

4

2.2. Constitutive rule of fastener plasticity

The behavior of the fastener is modeled by connecting EP-KIN and L material in series (see Figure A.19a). The threshold value of the L material is set to the yield strength f_{sy} of the EP-KIN material. Figure A.19 illustrates the simulated monotonic and hysteresis behavior of the fastener model. The model captures variations in elastic stiffness before and after yielding, reflecting the embedding process of fasteners with reduced post-yielding stiffness compared with the initial stiffness (see Figure A.19b). Experimental results indicate that the initial loading stiffness $K_{initial-loading}$ is always smaller than the unloading stiffness $K_{unloading}$ (see A.19c). To model this phenomenon, a lock element is incorporated into the fastener model. The force contributed by the fastener under monotonic loading can be calculated refer to Shi et al. [36].

2.3. Constitutive rule of glubam crushing

A series combination of ±EP-ISO and ±STOP materials is used to model the crushing of glubam and the permanent deformation of the hole, as shown in Figure 1. This model is divided into tension-sided and compression-sided crushing, depicted in Figures 1 a and b, respectively. Specifically, three groups of +EP-ISO and TS materials were connected in parallel to simulate the tension-sided yield of the glubam, representing contact between the fasteners and the glubam hole during the tension-sided reloading/reverse loading stage. Similarly, three groups of −EP-ISO and CS materials are connected in parallel to model the compression-sided yield of the glubam, representing contact during the compression-sided reloading/reverse loading stage.

For TS material, the distance between the slider and the right end of the slot (upper limit) is set to the gap width G_{i+} ($i = 1, 2, 3$), while the distance to the left end (lower limit) is set to a large value, making it unattainable (e.g., 30 mm). The simulated monotonic and hysteresis behavior of tension-sided glubam crushing are illustrated in Figures 1 c and e. For CS material, the distance between the slider and the left end of the slot (upper limit) is set to the gap width G_{i-} ($i = 1, 2, 3$), with the right end distance similarly selected as an unattainable value. The behavior of compression-sided glubam crushing is shown in Figures 1 d and f. Therefore, the TS and CS materials retain details about the irrecoverable deformation of glubam and the contact status between the fastener and glubam on the tension and compression sides, respectively.
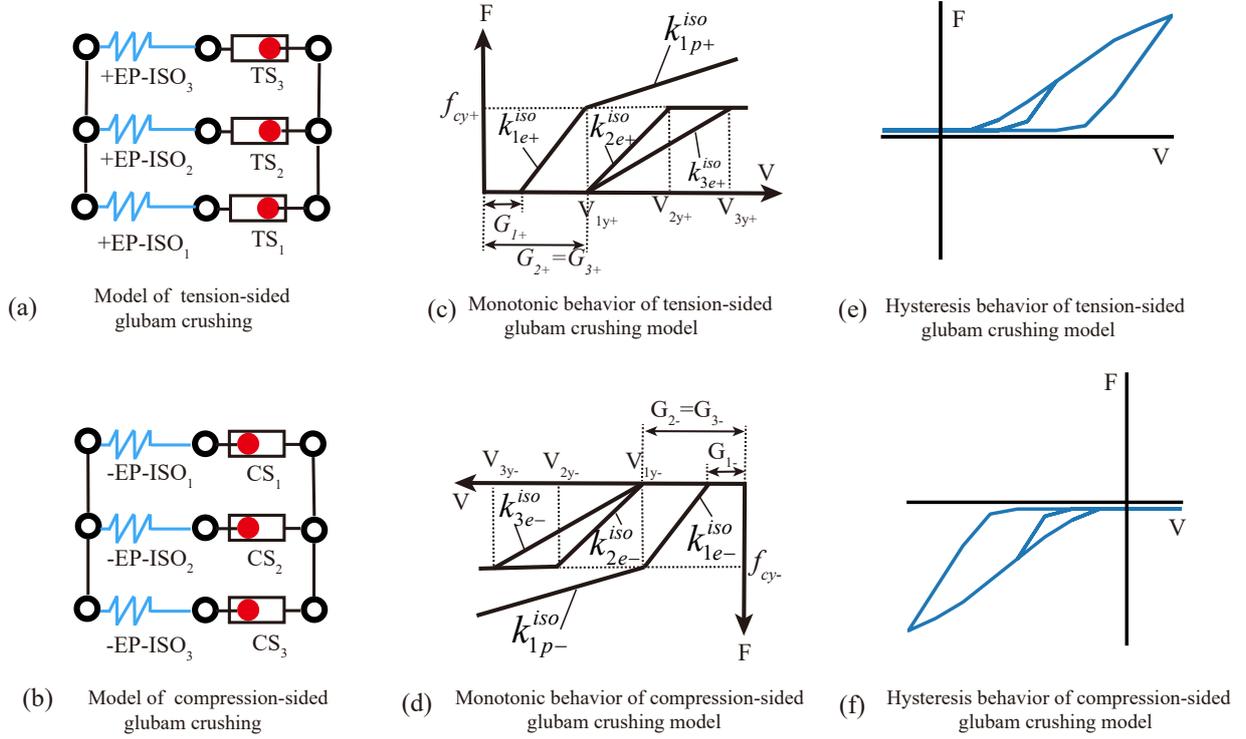
Figure 1: Constitutive rule of glubam crushing model: configuration of glubam crushing model (a and b), monotonic behavior of glubam crushing model (c and d) and hysteresis behavior of glubam crushing model (e and f). (modified based on Shi et al. [37])

Two assumptions formulate the basis of the glubam crushing model, namely (i) the yield strengths for $\pm EP-ISO_1$, $\pm EP-ISO_2$ and $\pm EP-ISO_3$ are equal, (ii) $\pm EP-ISO_2$ and $\pm EP-ISO_3$ are elasto-perfect plastic. These assumptions allow for a gradual elasto-plastic transition in the force-slip curve and enable the loading and unloading stiffness to be set as unequal. Based on the aforementioned model and assumptions, the resistance force generated by the glubam crushing action can be calculated using the following equations. Compared with Shi et al. [36], these equations reflects the asymmetry of tension and compression sides.

$$F_{c\pm}(V) = \Sigma F_{i\pm}(V) \qquad (i = 1, 2, 3) \tag{1}$$

$$F_{i\pm}(V) = 0 \qquad (\mid V \mid < G_{i\pm}) \tag{2}$$

$$F_{i\pm}(V) = k_{ie\pm}^{iso}(V - G_{i\pm}) \qquad (G_i < \mid V \mid < V_{iy\pm}) \tag{3}$$

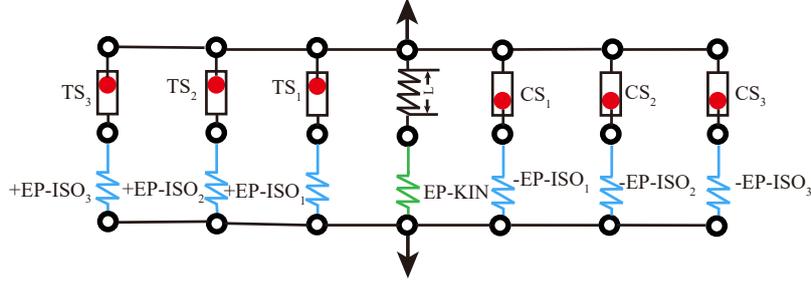$$F_{i\pm}(V) = k_{ip\pm}^{iso}(V - V_{iy\pm}) + f_{cy\pm} \qquad (\mid V \mid > V_{iy\pm}) \tag{4}$$

6

Figure 2: Proposed asymmetric pinching damaged (APD) hysteresis model for joints (modified based on Shi et al. [37])

where $F_{i\pm}$ is the force generated by the i th combination of $\pm$EP-ISO and $\pm$STOP materials in glubam crushing model, $G_{i\pm}$ is the gap of the $STOP_{i\pm}$ material, $V_{iy\pm}$ is the yield displacement of the i th combination of EP-ISO and STOP materials in glubam crushing model, $k_{ie\pm}^{iso}$ is the elastic stiffness of the $\pm EP - ISO_i$ material, $k_{ip\pm}^{iso}$ is the post-yield stiffness of the $\pm EP - ISO_i$ material ($k_{2p\pm}^{iso} = k_{3p\pm}^{iso} = 0$), and $f_{cy\pm}$ is the yield strength of the $\pm EP - ISO_i$ material.

2.4. Constitutive rule of joint model

The glubam joints are represented by a series of two-dimensional axial connector elements, CONN2D2, available in ABAQUS. Each element is assigned with basic material behaviors, including elasto-plastic (EP material model), STOP (S material model), and LOCK (L material model) behaviors. In this joint model, all nodes are positioned at the same location, and the mechanical behaviors are assigned exclusively to the tension and compression degree of freedoms (DOFs) of the connector elements. As mentioned earlier in this section, the contributions of the steel bolt and glubam bearing are modeled individually, and the overall behavior of the joint is a parallel superposition of the actions contributed by the fastener and glubam. The schematic of the overall joint model is shown in Figure 2. The proposed model effectively represents three typical features observed in the hysteresis behavior of glubam joints: pinching, asymmetry, and strength degradation.

2.4.1. Pinching

As loading increases, the bamboo fibers are crushed by the fastener. Due to the irreversible nature of fiber crushing, the affected glubam area cannot provide an immediate response in subsequent loading cycles. This slack leads to a delay in the connection response and reduces the stiffness each connector provides [4]. This effect is reflected in the hysteresis as 'pinching,' one of the most recognizable nonlinear features of wood-based structures. To model this pinching phenomenon, TS and CS materials were used to capture the irrecoverable deformation of glubam.

2.4.2. Asymmetry

As discussed before, various circumstances increasingly prevalent in structural design can cause significant deviations from the symmetrical hysteretic behavior of glubam members (e.g., [36]), resulting in notably asymmetrical responses. Three common scenarios exemplify such asymmetry: (i) assemblies subjected to lateral-axial load combinations (e.g., shear walls of lower stories), resulting in an asymmetrical displacement response [5]; (ii) hybrid connections integrating glubam members with stiffer and thicker materials (e.g., concrete, steel plates, and multilayered gypsum boards), leading to fastener fixation on one side of the shear plane accompanied by strong frictional forces, known as the "rope effect" (particularly evident in concrete). This phenomenon generates a pronouncedly asymmetrical force response [9, 6, 7, 8]; and (iii) overturning anchorage systems (e.g., hold downs, steel angle brackets, and Anchor Tie-down Systems (ATS)), which exhibit an asymmetric tensile/compressive behavior (termed taxonomic asymmetry), characterized by hysteresis only in tension and a stiff quasi-linear response in compression [10, 11, 12]. In the proposed joint model, the tension-sided and compression-sided crushing model were combined in parallel, thus modeling each side of hysteretic responses separately. When overlaying these two contributions, the asymmetrical responses presented in the hysteresis responses can be modeled.

2.4.3. Damage (Strength degradation)

To model the strength degradation presented in the hysteresis behavior, a damage criterion was introduced into the $+EP-ISO_1$ and $-EP-ISO_1$ material to model the force descending stage of tension side and compression side, respectively. As shown in Figure 3 a and b, two threshold values (F_{d+} and F_{d-}) and two damage indexes (I_{d+} and I_{d-}) was introduced to define the damage initiation and end points. The resulted hysteresis behavior after incorporating damage criterion were illustrated in Figure 3 c and d. With this damage behavior, the resistance force generated by the combination of $\pm EP-ISO_1$ and $\pm STOP_1$ materials can be calculated using the following equations:

$$F_{1\pm}(V) = 0 \qquad (\mid V \mid < G_{1\pm}) \tag{5}$$

$$F_{1\pm}(V) = k_{1e\pm}^{iso}(V - G_{1\pm}) \qquad (G_{1\pm} < \mid V \mid < V_{1y\pm}) \tag{6}$$

$$F_{1\pm}(V) = k_{1p\pm}^{iso}(V - V_{1y\pm}) + f_{cy\pm} \qquad (V_{1y\pm} < \mid V \mid < V_{d\pm}) \tag{7}$$

$$F_{1\pm}(V) = k_{d\pm}(V - V_{d\pm}) + I_{d\pm} * F_{d\pm} \qquad \mid V \mid > V_d \tag{8}$$
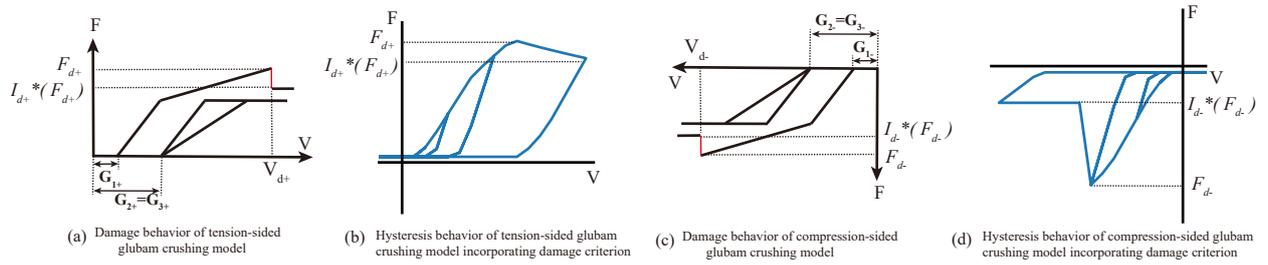
Figure 3: Damage behavior of glubam crushing model. (modified based on Shi et al. [37])

3. Automatic identification of APD hysteresis model parameters

To simulate the complex behaviors of glubam joints, the proposed model incorporates numerous flexible parameters, making automatic parameter calibration essential. To enhance the model's practical value, this study investigates and compares three methods for parameter identification: (i) PGA, (ii) BI, and (iii) BNN-PGA. The first two methods have already been proposed and validated in existing studies (Shi et al. [37, 38]), and therefore, they will only be briefly described in this section. However, the parameter tuning, comparison of PGA and GA, and the estimated parameter distributions in BI-based identification, are the original works completed in this study and will be discussed in detail.

3.1. Parameter tuning and comparison of PGA and GA

The rough determination of parameters involves extraction of the characteristic points and parameters of the hysteresis curves from the tested results (i.e. the stiffness, K, and the yield slip, V_y). The yield point is determined according to BS EN 12512:2001 [39]. A more advanced method to calibrate the yield point is proposed in [40, 37], which is more suitable for a bi-linear load-deformation response. After determining these key points, following similar procedures and principles in [36, 40], the model parameters controlling the hysteresis curves can be calibrated manually. Noting that the parameters for positive and negative sides should be identified separately to reflect the asymmetry.

Based on the rough parameter obtained above, a more precise procedure is further developed for parameter identification. Genetic algorithms (GA) is a well-known optimization algorithm based on fitness function evaluation, recombination, mutation and individual selection of the next generation [41, 42]. GA are widely used in many fields, but often require too much time and repetitive evaluation. The most time-consuming operation within GA is the evaluation of the fitness function [43, 44]. Hence, an effective and efficient PGA algorithm is developed in [36] based on a master-slave configuration based parallel programming structure. Some procedures need to be carried out serial (recombination, mutation and selection operators) are only executed in the master thread, while the other CPU cores are parallel adopted for fitness evaluation of the
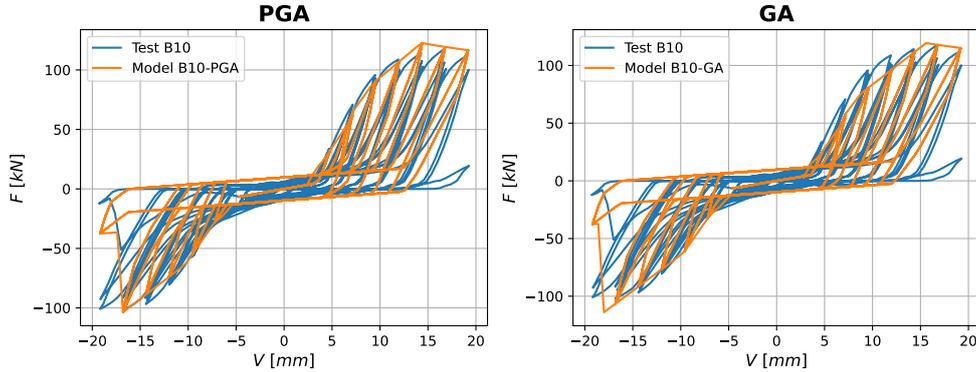
9

Figure 4: Comparison of identification accuracy for PGA and traditional GA.

design population, which does not require inter-cores communication. The parallel execution of the solution algorithm is schematically depicted in Figure B.20 [45]. More details are introduced in [36].

To mitigate convergence issues associated with PGA in complex optimization problems, a careful tuning of parameter setting of the PGA, such as mutation rate, crossover rate, population size and generation number has been carried out to improve convergence. Preliminary tuning identified that the optimal convergence is achieved with a crossover probability of 0.8, a mutation probability of 0.08, a population size of 30, and a total generation of 50. After the rough determination of model parameters, an amplification factor of 10 and a reduction factor of 0.2 for the estimated values of all parameters are chosen as the upper and lower bounds of the search space. Rough estimation of model parameters and constraining the search space can similarly enhance the convergence of the optimization process. In each generation, 30 slave threads evaluate 30 individuals simultaneously, with one processor core assigned to each thread. The random initialization of the GA population can lead to variability in the solutions across different runs. However, through extensive trials, we determined that using the specified parameter settings reliably leads to convergence towards a near-optimal solution while maintaining high identification efficiency. This configuration also minimizes redundant iterative computations, as increasing the number of generations beyond a certain point provides only marginal improvements in accuracy. The PGA was terminated based on a maximum number of generations. These criteria were chosen to ensure a balance between computational efficiency and solution quality. The computational tasks were executed using two Intel(R) Xeon(R) Silver 4310 CPUs, with 24 cores and 48 logical processors in each, which enabled efficient execution of the parallel genetic algorithm.

The proposed PGA was compared with the traditional GA regarding identification accuracy and efficiency, as shown in Figure 4 and Table 1. The searching space defined by the traditional GA is consistent with that of the PGA. The Relative Root Mean Square Errors (RRMSE) (see Eq.9) was used herein to evaluate the identification accuracy. From Table 1, it can be seen that the PGA and the traditional GA exhibit comparable identification accuracy. Meanwhile, the PGA significantly enhances identification efficiency.
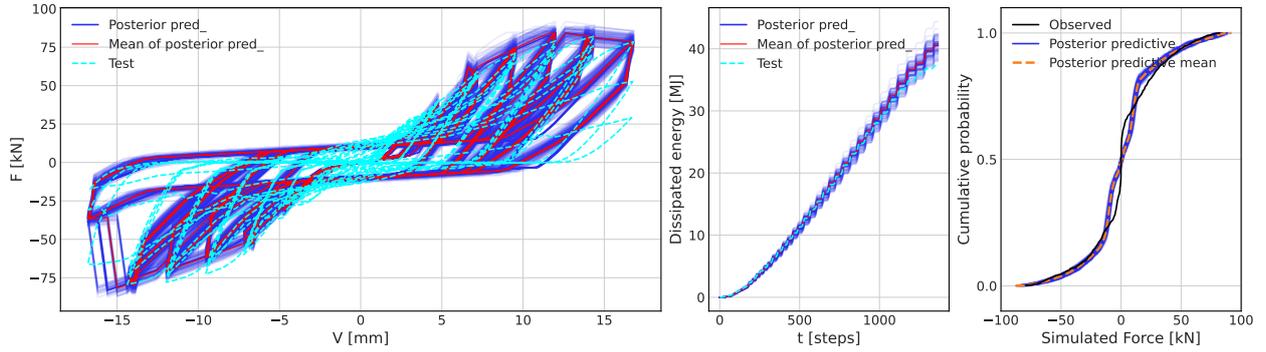
Table 1: Comparison of the traditional GA and PGA.

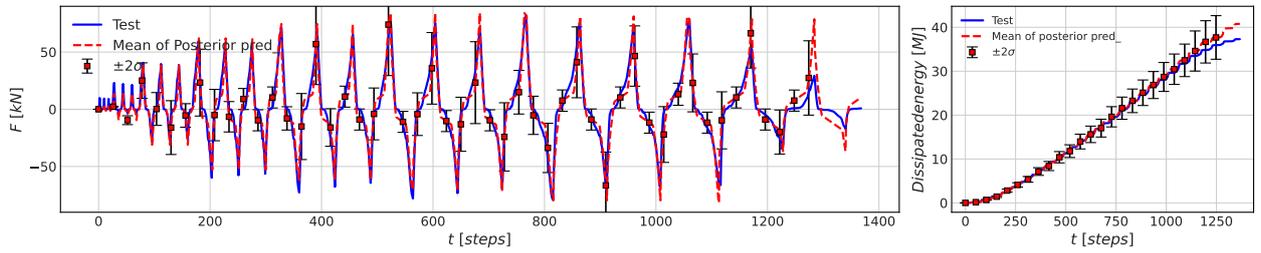| Method	PGA	Traditional GA
Accuracy	$RRMSE$=8.32%	$RRMSE$=8.95%
Computation cost	Around 25 min	Around 11 h
Evaluation times	1500	1500
Overall Efficiency	High	Low

3.2. BI-based identification and estimated parameter distributions

Following the procedures proposed in [38], we employ Sequential Monte Carlo (SMC) as a method to address this issue by sampling the joint posterior distribution. By tempering the posterior, this algorithm can partially avoid getting trapped in local optima and achieve better convergence. This approach is particularly useful in dealing with multimodal and non-convex problems.

To mitigate convergence issues associated with BI in complex optimization problems, informative priors were incorporated to constrain the parameter space and smooth the posterior landscape, making it easier for the SMC algorithm to converge. Selecting proposal distributions that are closer to the target posterior distribution can significantly enhance convergence. In this study, truncnormal distribution with mean values equal to the roughly determined parameters values discussed in section 3.1 was chosen as the prior distribution. An amplification factor of 3.0 and a reduction factor of 0.1 for mean values of all the parameters are selected as the upper bound and lower bound of the truncnormal distribution. 0.5 times the mean values are selected as the standard deviations of the prior distributions. To quantify the estimated uncertainty, the bounds of the response were calculated based on the posterior distribution of the APD model parameters. 100 sets of model parameters were generated from posterior distribution and their corresponding standard deviation σ was calculated. The generated parameter sets were inputted into the APD model to obtain corresponding output responses under cyclic loading conditions, as illustrated in Figure 5.

(a) Posterior prediction of hysteretic curve, energy dissipation and cumulative probability of simulated force values.

(b) Time history and standard deviation of the predicted force and energy dissipation

Figure 5: Comparison of the test result and 100 posterior sample under cyclic loading.
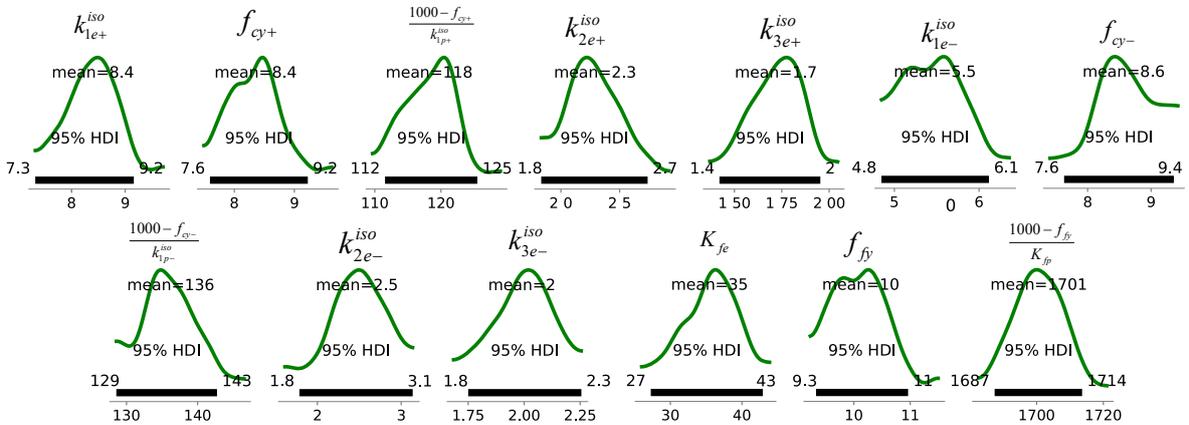

Figure 6: Mean values of the posterior SMC samples and the detailed marginal posterior PDF of each parameter

After synthesizing the response data for 100 groups, the statistical measures, specifically the mean and standard deviation (σ), were calculated. Figure 5 b compares the mean values of these 100 samples with the prior data, with error bars representing $\pm 2\sigma$. Generally, the output bounds encompassed the test data, indicating that the estimated parameters closely represent the true parameter values. As shown in Figure 5 a, the comparison of hysteresis curves and energy dissipation history demonstrates that the posterior data
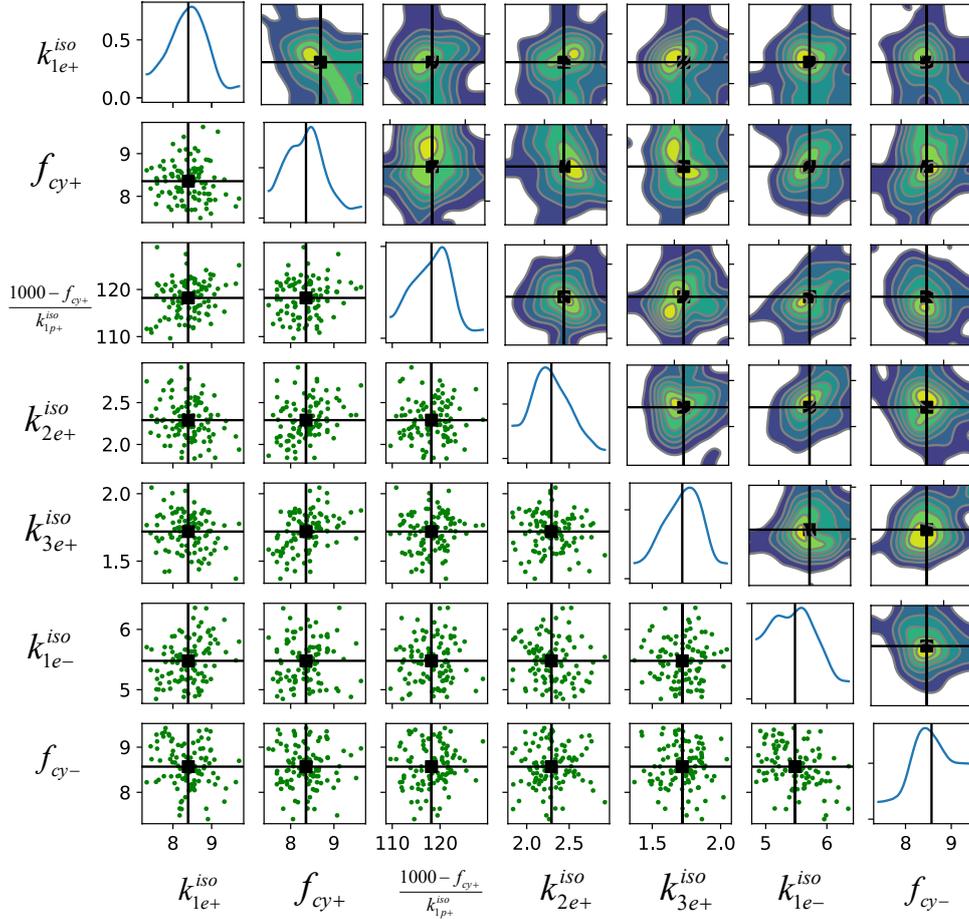
12

Figure 7: Pair plot using posterior samples of 7 representative inferred parameters obtained using SMC.

effectively captures the key features of the test data.

The mean values of the posterior SMC sample parameters and the detailed marginal posterior probability density functions of selected parameters are shown in Figure 6. Figure 7 displays the pair plot for seven representative inferred parameters, constructed from posterior samples derived via SMC. On the diagonal, the plots depict the kernel density estimates for the marginal PDFs of each parameter. Below the diagonal, the plots illustrate the posterior samples within the parameter pair space, and the contour plots of the kernel density estimates are presented above the diagonal.

3.3. BNN-PGA coupling parameter identification

The proposed PGA method offers significantly improved computational efficiency over the traditional serial GA. However, like other heuristic algorithms, PGA still necessitates computing a large number of cases. This is especially challenging for hysteretic models with high computational demands, where the optimization efficiency remains sub-optimal. To address this issue, this section introduces an innovative

13

method that combines the strengths of BNN (Graves [30], Blundell et al. [31]) with PGA. BNNs effectively merge Bayesian statistics with neural networks, offering a probabilistic interpretation of the model prediction process and enabling the quantification of prediction uncertainties, which is a feature absent in traditional neural networks. By incorporating the uncertainty quantification from BNN predictions, it is possible to forego the creation of a large-scale training dataset, which considerably reduces the computational load and enhances the practical value of the proposed method. Consequently, BNNs are increasingly applied in fields such as reliability analysis and structural response prediction (Perez-Ramirez et al. [46], Dang et al. [47], Wang et al. [48]).

Within the basic principles of BNN, Monte Carlo Dropout is a notable technique (Gal and Ghahramani [49, 50]). It involves applying dropout not just during training, but also during inference, to simulate the sampling from a posterior distribution. This method allows for multiple stochastic forward passes through the network, with dropout serving to create a resampled weight combination each time, thus enabling the estimation of the uncertainty in the network predictions. Compared with other implementation manner of BNN such as Bayes by Backprop, Stochastic Gradient Langevin Dynamics, and Kronecker-Factorised Laplace, Monte Carlo Dropout is simpler to be integrated into various neural network architectures without necessitating significant modifications to their structure or optimization processes. Thus, it has been selected as the BNN implementation method for this study.

3.3.1. Framework of BNN-PGA

The overall framework of the coupling BNN-PGA is shown in Figure 8. It can be separated into four different parts:

(1) Part 1: Generation of parameter combinations

This part adheres strictly to the principles of the traditional GA. The initial populations for the first generation are randomly generated within predefined upper and lower limits. For subsequent generations, processes such as crossover, recombination, and potential mutation are employed to develop new populations from the selected samples of the preceding generation.

(2) Part 2: BNN training

Frequently, the parameter identification process using PGA is iterated multiple times to assess the impact of key configurations, reduce fluctuations, and enhance the accuracy of the final results. This iterative process effectively serves as data preparation for BNN training, eliminating the need to generate a large dataset for BNN only. The parameter combinations and their corresponding fitness values are recorded, and are used as the inputs and outputs for the BNN, respectively. Once the BNN model is well-trained, it is integrated into the PGA-based optimization process. The inference results for each parameter combination, including mean value and standard deviation, are used as the basis for fitness calculation and parameter selection in subsequent steps.
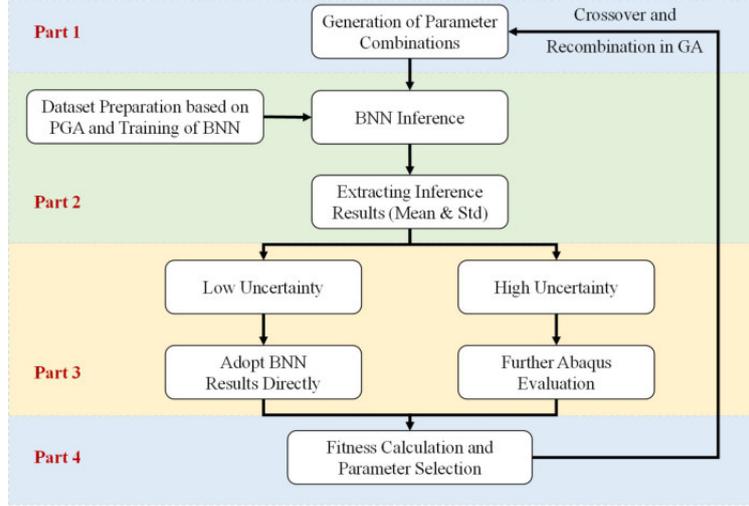
14

Figure 8: Framework of the proposed BNN-PGA method

(3) Part 3: Uncertainty quantification

The uncertainty of the inference results is quantitatively assessed by the ratio of the predicted standard deviation to the mean value. High uncertainty results prompt further evaluation of the corresponding parameter combinations using the ABAQUS model in a parallel manner. Conversely, for results with low uncertainty, the mean fitness value from the BNN inference is directly utilized. Notably, in critical generations such as the last generation, all parameters are evaluated using ABAQUS to enhance reliability.

(4) Part 4: Fitness value calculation and parameter selection

Following part 3, fitness values for all populations in the current generation are obtained either through the mean square error between the ABAQUS simulation results and experimental data or via BNN inference. The optimal parameter combination is then selected to form the basis of the next generation.

3.3.2. Key settings and BNN model evaluation

In this study, the optimization process using BNN-PGA employs a Multi-Layer Perceptron (MLP) (Rosenblatt [51], Haykin [52]), also known as a fully connected neural network, as the foundational network architecture. This structure is implemented using PyTorch and is chosen for its efficiency in both training and inference stages. It is adept at establishing the required mapping relationship between the 20-dimensional vector inputs (key parameters in the proposed numerical model) and the 1-dimensional scalar output (prediction MSE corresponding to this parameter combination). Given that each input dimension operates independently, there is no need for selecting recurrent architectures such as Long Short-Term Memory networks (LSTM) or Gated Recurrent Units (GRU), nor for iterative architectures like Temporal Convolutional Networks (Hochreiter and Schmidhuber [53], Cho et al. [54], Xu et al. [55, 56], Gu et al. [57]). Moreover, more complex networks such as the Transformer, and its modifications like Reformer and
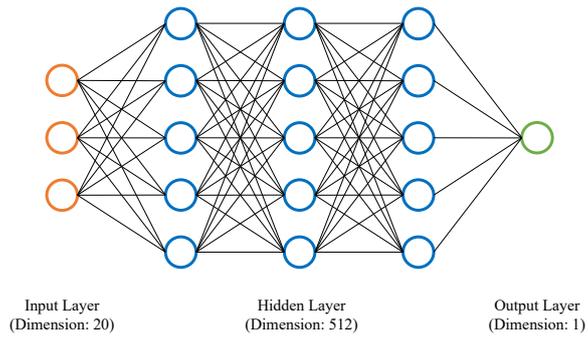
15

Table 2: Key hyperparameters in BNN

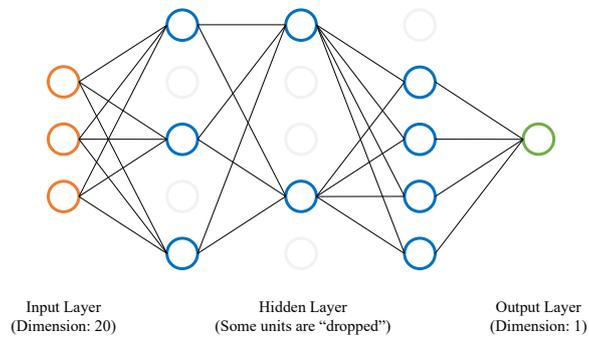| Name	Value	Description
Dataset size	6,500	The total number of samples for BNN
Dataset separation	-	Training: 70%; Validation: 20%; Testing: 10%
Number of layer	3	The number of hidden layers in BNN
Dropout ratio	0.5	Dropout ratio in Monte Carlo dropout processes
Sample time	5	The number of repetitive dropout processes adopted for uncertainty quantification
Hidden unit	512	The dimension of hidden unit in BNN
Initial learning rate	0.0002	The initial learning rate adopted in BNN training

Informer, as well as TimesNet, are not considered due to the limited size of the available training dataset and the goal of maintaining high efficiency (Vaswani et al. [58], Kitaev et al. [59], Zhou et al. [60], Wu et al. [61]). The foundational theories of MLP, thoroughly discussed in the provided references, will not be reiterated here.

During the training and validation phases, different architectural settings, particularly the number of hidden layers and the neuron count in each layer, are meticulously compared. Some key hyperparameters of the adopted BNN are provided in Table 2. The typology of the active BNN model and BNN model after Monte Carlo dropout are provided in Figure 9. During the training process of the neural network, the training and validation loss are continuously monitored. If the validation loss does not decrease for several epochs (e.g., 50), the neural network training can be terminated and the model with the minimum validation loss is regarded as the "well-trained" model. The following methods are adopted for controlling the overfitting: (1) Searching for optimal hyperparameters based on cross-validation; (2) Monitoring the validation loss continuously; (3) Exponential learning rate decay; and (4) Proper dropout during the training and inference processes. Noting that, the overfitting cannot be completely eliminated during the inherent property of the neural networks and highly non-convex of the optimization problem itself. However, the aforementioned measures are valuable in controlling the effect of overfitting and can support the obtaining the acceptable results presented in Table 3.

In this study, the BNN training utilizes a dataset of 6,500 samples, generated from PGA parameter identification cycles. The training process for the BNN model is efficient, taking less than 10 minutes. The performance of the optimally trained BNN model is detailed in Figure 10. The results indicate that approximately 70% of the samples exhibit a relative deviation of less than 20%. However, 7.6% of the samples show a relative error exceeding 40%. A trade off between dataset construction burden and absolute model accuracy is the main reason of adopting such a BNN model as the final model without further accuracy improvement.

16

Input Layer
(Dimension: 20)

Hidden Layer
(Dimension: 512)

Output Layer
(Dimension: 1)

(a) Active BNN

Input Layer
(Dimension: 20)

Hidden Layer
(Some units are "dropped")

Output Layer
(Dimension: 1)

(b) BNN after Monte Carlo dropout (the "dropped" neurons are selected randomly)

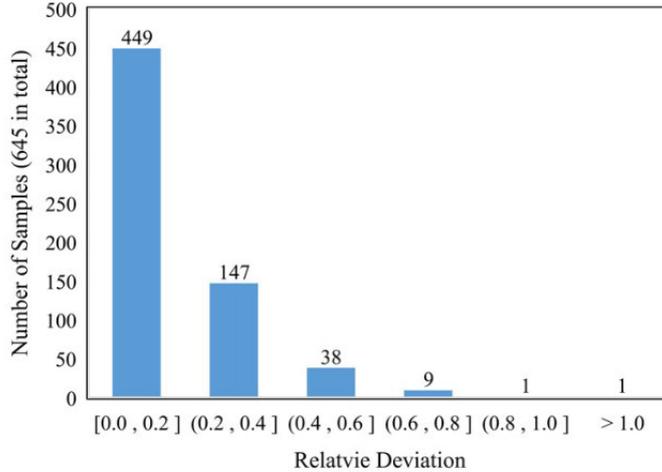Figure 9: The typology of the BNN model before and after Monte Carlo dropout

Figure 10: Distribution of relative distribution on the testing dataset

Table 3: BNN-PGA optimization results and comparison

Type	Threshold (Std / Mean Value)	Time (s)	Time reduction (%)	Best fitness value (MSE) in the last generation
Pure PGA (ABAQUS simulation only)	-	45382	-	86.7
	0.5	47248	-4.1	78.2
BNN-PGA	1.0	28665	36.8	100.7
	1.5	10680	76.5	164.9
BNN only	-	5257	88.4	197.7

3.3.3. BNN-PGA optimization performance

In the implementation of BNN-PGA, if the ratio between the standard deviation and mean value of the predicted fitness values are less than a certain threshold (discussed in Table 3), the BNN inference results will be directly adopted. In addition, for the last one in every 10 generations and the final evaluation generation, all parameter combinations will be evaluated through ABAQUS simulation to improve the reliability of optimization. The functions adopted for fitness evaluation is mean square error (MSE). The results of BNN-PGA optimization and comparison with pure PGA method is provided in Table 3. "Std" and "Mean Value" represent the standard deviation and mean value calculated based on the results of multiple BNN predictions, and the ratio between them are adopted for measuring the prediction uncertainty. It can be seen that, even with limited BNN model accuracy, the proposed BNN-PGA method still reaches similar performance with the pure PGA parameter identification. This achievement highly relies on the uncertainty quantification, for the optimization process based on the mean predicted MSE only fails in reaching similar accuracy. In terms of efficiency, the overall parameter time can be reduced by 36.8% with a threshold of 1.0.

Despite its similar accuracy and higher efficiency, the BNN-PGA method has significant room for improvement, particularly since the accuracy of the BNN model can continually improve as more samples are

18

accumulated. Additionally, this method is particularly well-suited for large-scale designs or simulations. In large-scale simulations, the accumulation of available samples accelerates, leading to a more reliable BNN model, which in turn could improve the overall time reduction ratio. Furthermore, the inference time for BNN does not vary significantly with an increasing simulation scale, whereas PGA simulations based on ABAQUS (or other finite element software) generally take more time. Consequently, the advantages of the BNN-PGA method become more pronounced as the scale of the simulation increases.

4. Validation of APD hysteresis model

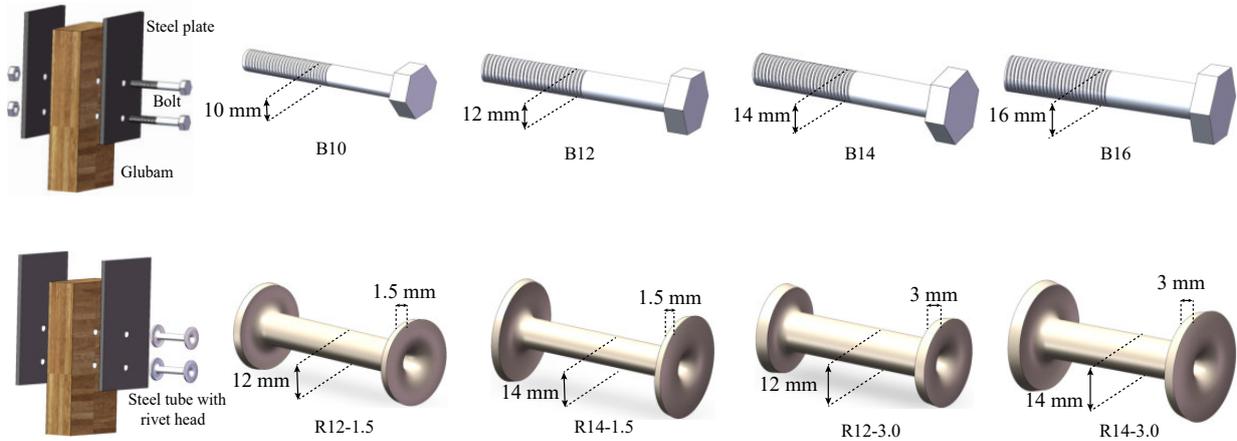### 4.1. Experimental benchmark tests for model validation

Figure 11: Configuration of glubam joints. (modified based on [37, 62])

The experimental benchmarks for APD hysteresis model validation comprised eight groups of cyclic test results of glubam connections including two joints types: (i) bolted connections and (ii) riveted connections with hollow steel tube. Adopting experimental data from two types of joints with different features helps improve the reliability of validation. Detailed configurations about the studied joints are illustrated in Figure 11. For riveted connections with hollow steel tube, the thickness and outer-diameter of steel wall were accounted as the variables resulting in 4 configurations: R12-1.5, R14-1.5, R12-3.0 and R14-3.0. For bolted connections, the diameter of bolt was accounted as the variables resulting in 4 configurations: B10, B12, B14 and B16. The tested hysteresis behaviors were illustrated in Figure 12 These data are obtained from the experiments finished by the authors previously [37, 62].

4.2. APD hysteresis model response

The optimal parameter combinations of APD model for the 8 experimental benchmark tests are obtained following the framework proposed in Section 3. The model parameters were first roughly determined in
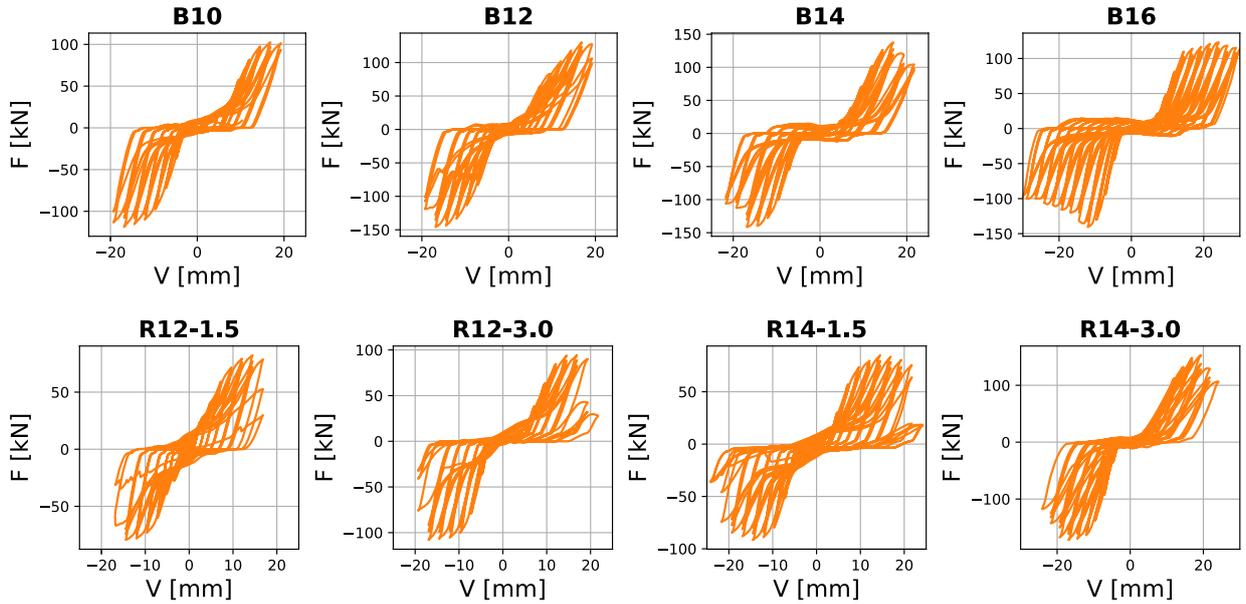
Figure 12: Cyclic test results of two types of glubam connections. (modified based on [37, 62])

Section 3.1, and then an amplification factor 10 and a reduction factor 0.1 for roughly determined parameter values are selected as the upper bound and lower bound of the searching space of parallel genetic algorithms. The population size and generation number are chosen as 50 and 50, thus a total of 2500 evaluations are performed. 25 slave threads are arranged to evaluate 25 individuals simultaneously in each generation and 1 processor is distributed to execute each thread. The optimal predicted hysteretic behavior and energy dissipation-time history for the 8 benchmark tests are illustrated in Figure 13. It can be observed the proposed model can fit the pinching, damage and asymmetric behavior very well, and the energy dissipation also achieve a good fit between the tested and predicted values.
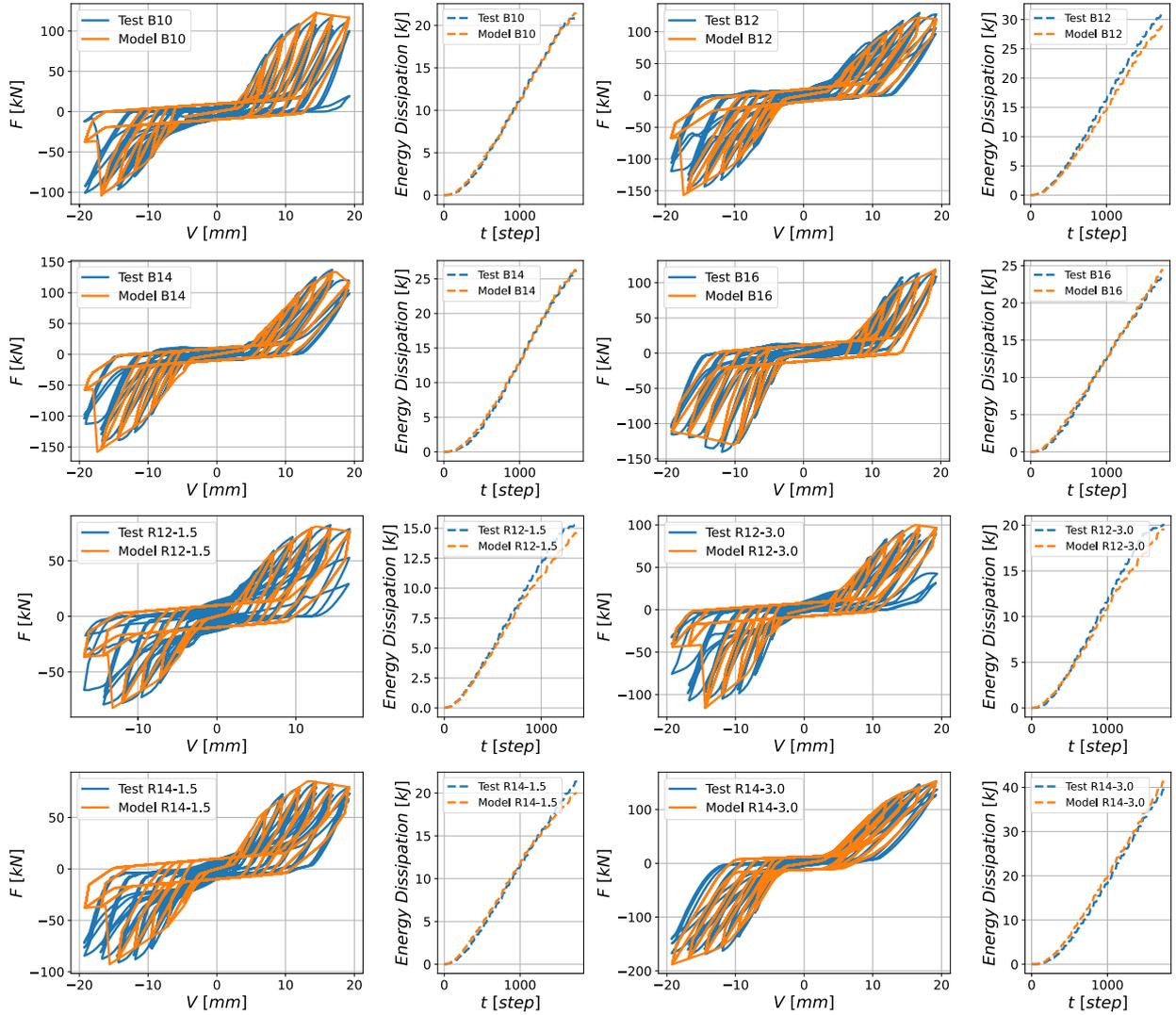
Figure 13: Comparison of the hysteretic responses from the tests and the optimal APD model prediction.

4.3. Comparison with other hysteretic models

The predicted responses by the APD hysteresis model are also compared with three well-known hysteretic models available in the literature. These models are: (i) the SAWS model (or more called MSTEW) of Stewart [63] and later modified by Folz & Filiatrault [64]; (ii) the Pinching4 model of Lowes et al. [65]; and (iii) the DowelType model of Dong et al. [66]. These three models are available in the OpenSees software, where the first two are commonly used to simulate timber connections, and the latter is recently incorporated into this software.

Figure 14 and 15 compare the force–displacement hysteresis of the four models for the 8 benchmark tests. To quantitatively compare the prediction accuracy of different models, the predicted response is compared

21

Table 4: $RRMSE$ (see Eq.9) between tested response and predicted response.

Model	Configuration							
	B10	B12	B14	B16	R12-1.5	R14-1.5	R12-3.0	R14-3.0
APD	8.32%	13.38%	7.56%	9.75%	12.42%	10.21%	18.32%	13.15%
Saws	17.64%	25.31%	21.44%	32.21%	16.15%	15.43%	23.25%	28.61%
Pinching 4	12.64%	16.32%	13.45%	12.58%	16.12%	18.33%	14.41%	23.56%
DowelType	7.65%	14.72%	9.53%	8.34%	6.63%	8.32%	10.28%	10.31%

with the tested responses using the Relative Root Mean Square Errors (RRMSE), as shown in Table 4. The RRMSE provides a measurement of the error between two signals, $\mathbf{a}$ (tested value) and $\mathbf{b}$ (predicted value), and is defined as:

$$RRMSE\left(\mathbf{a}, \mathbf{b}\right) = \frac{\sqrt{\left[\frac{1}{N_s} \sum_{i=1}^{N_s} \left(a_i - b_i\right)^2\right]}}{\sqrt{\left[\frac{1}{N_s} \sum_{i=1}^{N_s} \left(a_i\right)^2\right]}} \times 100\left(\%\right) \tag{9}$$

where N_s denotes the total number of data samples in the signals.

Comparison shows that the APD model and DowelType gives the best fit among the four models in all cases, followed by the Pinching 4 model, while the SAWS model performed the worst fitting accuracy. According to the fitting results, It is verified the proposed APD model is capable of capturing all hysteresis features observed from the test including asymmetry, pinching, and damage behavior. The APD model proposed in this paper is able to consider the elastic, yielding, pinching, and failure behaviors of materials under cyclic loading, including the asymmetric hysteretic response observed under tension and compression. Consequently, this model is also applicable to materials other than glubam, provided they exhibit significant irreversible damage, as indicated by a pinching effect in the hysteresis curve during loading. The pinching effect in hysteresis behavior is commonly observed in materials and structural elements that experience degradation in stiffness and strength under cyclic loading, especially when there is damage or slip between components. This behavior is characterized by a narrowing or "pinching" of the hysteresis loops around the origin in a force-displacement or stress-strain relationships. For example, masonry structures, especially those without significant reinforcement or with poor mortar joints, can display pinching effects due to crack propagation and slippage at the mortar-brick interface under lateral cyclic loads. Wood and timber elements, particularly those with connections like nails, bolts, or dowels, can show pinching behavior due to the slippage of fasteners or crushing of wood fibers near the joints when subjected to cyclic loads. The APD model is also applicable to these materials.
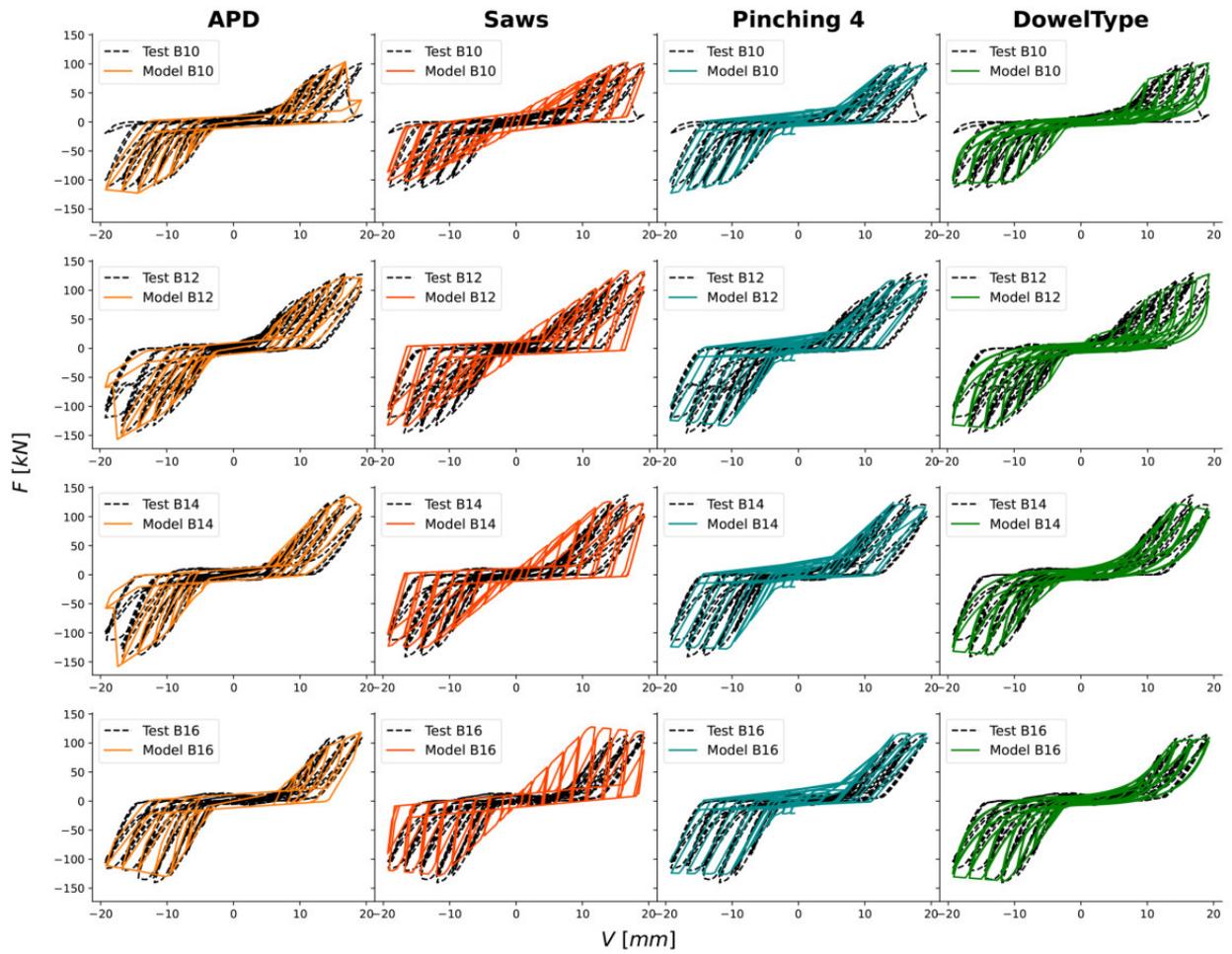
Figure 14: Comparison of force–displacement hysteresis between the experimental and prediction results of four models (APD, Saws, Pinching 4 and DowelType) (bolted connections).
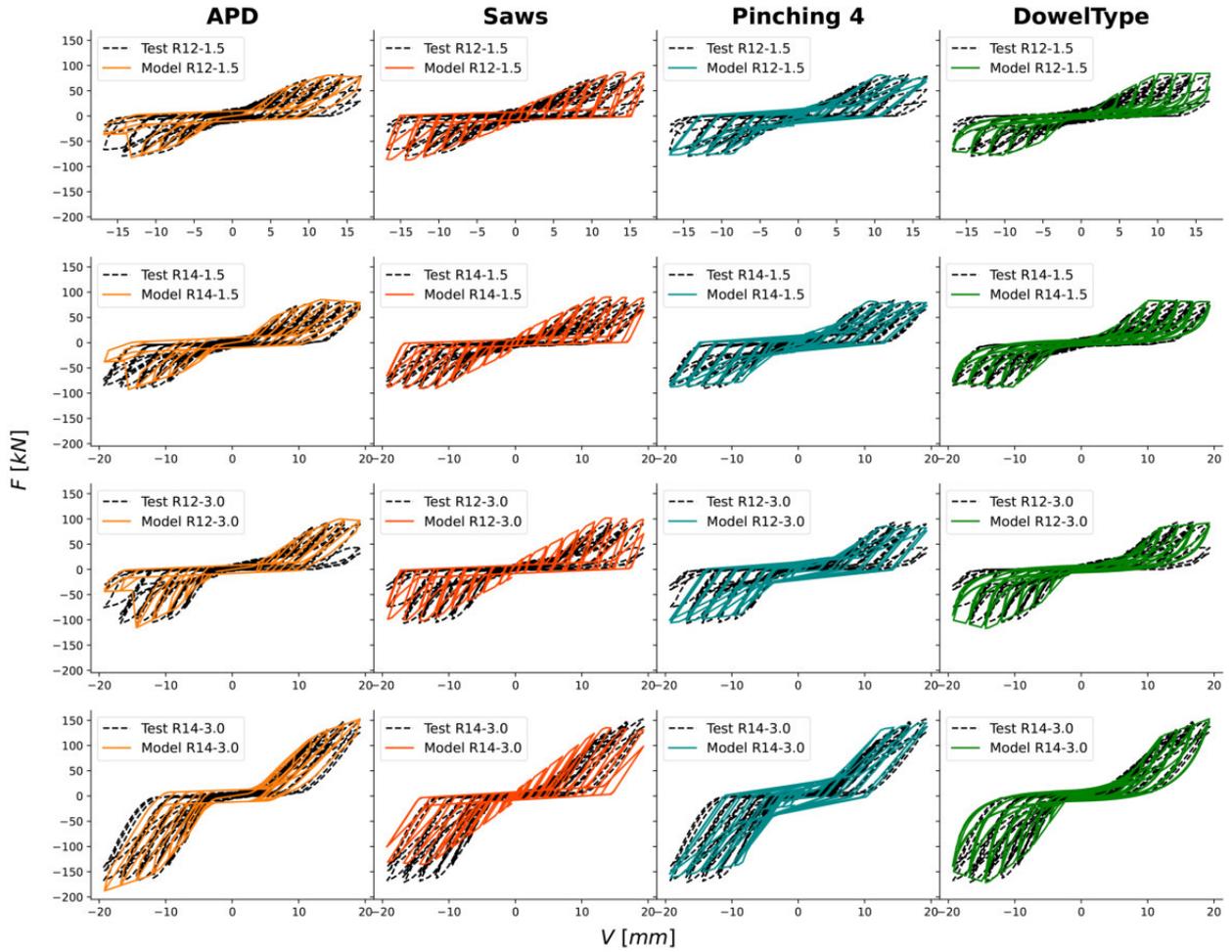
Figure 15: Comparison of force–displacement hysteresis between the experimental and prediction results of four models (APD, Saws, Pinching 4 and DowelType) (riveted connections).

5. Conclusions

This study develops a APD hysteresis model based on previous study for glubam members, complemented by identification frameworks designed for seamless integration with commercial finite element software ABAQUS. The calibrated model, following parameter identification, was compared and validated against a series of experimental glubam benchmark tests and three established hysteretic models (SAWS, Pinching4, and DowelType). The study yields the following conclusions:

(1) The proposed APD hysteresis model accurately captures the complex behaviors of glubam members, including asymmetry, pinching effects, and strength/stiffness degradation.

(2) Three parameter identification methods, PGA, BI, and BNN-PGA, are introduced, enhancing the capabilities of parallel numerical computation and parameter identification coupling BNN and finite element

24

models. These methods enable the automatic and precise identification of parameters in complex hysteretic models.

(3) Compared to three other well-known hysteretic models (SAWS, Pinching4, and DowelType), the APD and DowelType models consistently outperform the others in all test cases, underscoring its advantages in simulating the behaviors of glubam members.

Acknowledgments

Declaration of Competing Interest

The authors declare that they have no known competing financial interests or personal relationships that could have appeared to influence the work reported in this paper.

Data availability

The data that support the findings of this study are available from the corresponding author upon reasonable request.

References

[1] Y. Leng, M. Wang, Q. Xu, K. A. Harries, F. Zhang, K. Liu, Experimental study on longitudinal embedding performance of bolted engineered bamboo connections, Construction and Building Materials 411 (2024) 134730.

[2] M. Zhang, H. Fan, W. Li, H. Wu, Z. Yu, S. Zhao, Q. Zhou, C. Liu, Y. Li, H. Luo, A. Behnejad, G. Parke, Study on the elastic stiffness calculation method of single-bolted steel-bamboo scrimber-steel shear connections, Engineering Structures 301 (2024) 117331.

[3] A. Dauletbek, H. Li, R. Lorenzo, A review on mechanical behavior of laminated bamboo lumber connections, Composite Structures 313 (2023) 116898.

[4] N. Chan, A. Hashemi, P. Zarnani, P. Quenneville, Pinching-free connector for timber structures, Journal of Structural Engineering 147 (2021) 04021036.

[5] F. Guíñez, H. Santa María, J. L. Almazán, Monotonic and cyclic behaviour of wood frame shear walls for mid-height timber buildings, Engineering Structures 189 (2019) 100–110.

[6] L. Pozza, R. Scotta, D. Trutalli, A. Polastri, A. Ceccotti, Concrete-plated wooden shear walls: Structural details, testing, and seismic characterization, Journal of Structural Engineering 142 (2016) E4015003.

[7] J. Cao, H. Xiong, Z. Wang, J. Chen, Experimental investigation and numerical analysis for concrete-clt connections, Construction and Building Materials 236 (2020) 117533.

[8] R. Araya, J. Montaño, P. Guindos, Experimental test of the gap reinforced fastened connection (grfc): A highly stiff and ductile reinforced connection concept with reduced pinching for timber structures, Engineering Structures 251 (2022) 113584.

[9] A. Hassanieh, H. Valipour, M. Bradford, Load-slip behaviour of steel-cross laminated timber (clt) composite connections, Journal of Constructional Steel Research 122 (2016) 110–121.

[10] J. Schneider, E. Karacabeyli, M. Popovski, S. F. Stiemer, S. Tesfamariam, Damage assessment of connections used in cross-laminated timber subject to cyclic loads, Journal of Performance of Constructed Facilities 28 (2014).

[11] I. Gavrić, M. Fragiacomo, A. Ceccotti, Cyclic behaviour of typical metal connectors for cross-laminated (clt) structures, Materials and Structures 48 (2015) 1841–1857.

[12] X. Estrella, P. Guindos, J. L. Almazán, S. Malek, Efficient nonlinear modeling of strong wood frame shear walls for mid-rise buildings, Engineering Structures 215 (2020) 110670.

[13] Q. Xie, B. Zhang, L. Zhang, T. Guo, Y. Wu, Normal contact performance of mortise and tenon joint: theoretical analysis and numerical simulation, Journal of Wood Science 67 (2021) 1–21.

[14] P. A. Lacourt, F. J. Crisafulli, A. Mirasso, Finite element modelling of hysteresis, degradation and failure of dowel type timber joints, Engineering Structures 123 (2016) 89–96.

[15] J. Xu, J. D. Dolan, Development of nailed wood joint element in abaqus, Journal of Structural Engineering 135 (2009) 968–976.

[16] W. Pang, S. M. H. Shirazi, Corotational model for cyclic analysis of light-frame wood shear walls and diaphragms, Journal of Structural Engineering-asce 139 (2013) 1303–1317.

[17] G. Rinaldin, C. Amadio, M. Fragiacomo, A component approach for the hysteretic behaviour of connections in cross-laminated wooden structures, Earthquake Engineering & Structural Dynamics 42 (2013).

[18] L. Pozza, A. Saetta, M. Savoia, D. A. Talledo, Coupled axial-shear numerical model for clt connections, Construction and Building Materials 150 (2017) 568–582. URL: https://api.semanticscholar.org/CorpusID:113628457.

[19] M. Shahnewaz, S. Alam, T. Tannert, In-plane strength and stiffness of cross-laminated timber shear walls, Buildings (2018).

[20] L. Franco, L. Pozza, A. Saetta, M. Savoia, D. A. Talledo, Strategies for structural modelling of clt panels under cyclic loading conditions, Engineering Structures (2019).

[21] A. Sandoli, C. D'Ambra, C. Ceraldi, B. Calderoni, A. E. Prota, Role of perpendicular to grain compression properties on the seismic behaviour of clt walls, Journal of building engineering (2020) 101889.

[22] F. Ávila, P. Dechent, A. Opazo, Seismic behaviour evaluation of clt horizontal diaphragms on hybrid buildings with reinforced concrete shear walls, Engineering Structures 244 (2021) 112698.

[23] D. Shi, Y. Xu, C. Demartino, Y. Xiao, B. F. Spencer, Bio-based laminated truss structures with bolted steel connections: Experiment, modeling, and model-updating, Earthquake Engineering and Structural Dynamics (2023).

[24] M. He, J. Luo, D. Tao, Z. Li, Y. Sun, G. He, Rotational behavior of bolted glulam beam-to-column connections with knee brace, Engineering Structures 207 (2020) 110251.

[25] J. W. van de Lindt, M. Amini, D. R. Rammer, P. Line, S. Pei, M. Popovski, Seismic performance factors for cross-laminated timber shear wall systems in the united states, Journal of Structural Engineering (2020).

[26] D. Casagrande, S. Rossi, R. Tomasi, G. Mischi, A predictive analytical model for the elasto-plastic behaviour of a light timber-frame shear-wall, Construction and Building Materials 102 (2016) 1113–1126. SHATIS 2013 : Research on Timber Materials and Structures.

[27] C. Bedon, M. Fragiacomo, Numerical analysis of timber-to-timber joints and composite beams with inclined self-tapping

498   screws, Composite Structures (2019).

[28] M. Izzi, A. Polastri, M. Fragiacomo, Modelling the mechanical behaviour of typical wall-to-floor connection systems for cross-laminated timber structures, Engineering Structures 162 (2018) 270–282.

[29] M. Izzi, A. Polastri, M. Fragiacomo, Investigating the hysteretic behavior of cross-laminated timber wall systems due to connections, Journal of Structural Engineering-asce 144 (2018) 04018035.

[30] A. Graves, Practical variational inference for neural networks, Advances in neural information processing systems 24 (2011).

[31] C. Blundell, J. Cornebise, K. Kavukcuoglu, D. Wierstra, Weight uncertainty in neural network, in: International conference on machine learning, PMLR, 2015, pp. 1613–1622.

[32] G. Levitin, L. Xing, Y. Dai, Optimal loading of series parallel systems with arbitrary element time-to-failure and time-to-repair distributions, Reliability Engineering & System Safety 164 (2017) 34–44.

[33] O. A. Numanoglu, M. Musgrove, J. A. Harmon, Y. M. Hashash, Generalized non-masing hysteresis model for cyclic loading, Journal of Geotechnical and Geoenvironmental Engineering 144 (2018) 06017015.

[34] T. Wang, M. Noori, W. A. Altabey, Z. Wu, R. Ghiasi, S.-C. Kuok, A. Silik, N. S. Farhan, V. Sarhosis, E. N. Farsangi, From model-driven to data-driven: A review of hysteresis modeling in structural and mechanical systems, Mechanical Systems and Signal Processing 204 (2023) 110785.

[35] B.-H. Xu, A. Bouchaïr, M. Taazount, E. J. Vega, Numerical and experimental analyses of multiple-dowel steel-to-timber joints in tension perpendicular to grain, Engineering Structures 31 (2009) 2357–2367.

[36] D. Shi, G. C. Marano, C. Demartino, Bio-based connections and hybrid planar truss: A parallel genetic algorithm approach for model updating, Computers & Structures 301 (2024) 107463.

[37] D. Shi, G. C. Marano, C. Demartino, Modeling of glubam roof truss, parameter identification and updating based on parallel genetic algorithm, Engineering Structures 316 (2024) 118520.

[38] D. Shi, Z. Li, C. Demartino, Bio-based hybrid planar truss: Experimental testing, fe modeling and bayesian model updating, Engineering Structures 308 (2024) 117987.

[39] BS-EN-12512:2001, Timber structures-test methodscyclic testing of jointsmade with mechanical fasteners, 2001 (2001).

[40] D. Shi, C. Demartino, Z. Li, Y. Xiao, Axial load–deformation behavior and fracture characteristics of bolted steel to laminated timber and glubam connections, Composite Structures 305 (2023) 116486.

[41] G. C. Marano, G. Quaranta, J. Avakian, A. Palmeri, Identification of passive devices for vibration control by evolutionary algorithms, 2013.

[42] R. Greco, J. Avakian, G. Marano, A comparative study on parameter identification of fluid viscous dampers with different models, Archive of Applied Mechanics 84 (2014). doi:10.1007/s00419-014-0869-3.

[43] V. Skorpil, V. Oujezsky, P. Cika, M. Tuleja, Parallel processing of genetic algorithms in python language, in: 2019 PhotonIcs and Electromagnetics Research Symposium, 2019, pp. 3727–3731.

[44] O. Hasançebi, T. Bahçecioğlu, O. Kurç, M. Saka, Optimum design of high-rise steel buildings using an evolution strategy integrated parallel algorithm, Computers & Structures 89 (2011) 2037–2051.

[45] R. Cucuzza, M. Domaneschi, R. Greco, G. C. Marano, Numerical models comparison for fluid-viscous dampers: Performance investigations through genetic algorithm, Computers & Structures 288 (2023) 107122.

[46] C. A. Perez-Ramirez, J. P. Amezquita-Sanchez, M. Valtierra-Rodriguez, H. Adeli, A. Dominguez-Gonzalez, R. J. Romero-Troncoso, Recurrent neural network model with bayesian training and mutual information for response prediction of large buildings, Engineering Structures 178 (2019) 603–615.

[47] H. V. Dang, R. Trestian, T. Bui-Tien, H. X. Nguyen, Probabilistic method for time-varying reliability analysis of structure via variational bayesian neural network, in: Structures, volume 34, Elsevier, 2021, pp. 3703–3715.

[48] T. Wang, H. Li, M. Noori, R. Ghiasi, S.-C. Kuok, W. A. Altabey, Probabilistic seismic response prediction of three-

dimensional structures based on bayesian convolutional neural network, Sensors 22 (2022) 3775.

[49] Y. Gal, Z. Ghahramani, Bayesian convolutional neural networks with bernoulli approximate variational inference, arXiv preprint arXiv:1506.02158 (2015).

[50] Y. Gal, Z. Ghahramani, Dropout as a bayesian approximation: Representing model uncertainty in deep learning, in: international conference on machine learning, PMLR, 2016, pp. 1050–1059.

[51] F. Rosenblatt, The perceptron: a probabilistic model for information storage and organization in the brain., Psychological review 65 (1958) 386.

[52] S. Haykin, Neural networks: a comprehensive foundation, Prentice Hall PTR, 1998.

[53] S. Hochreiter, J. Schmidhuber, Long short-term memory, Neural computation 9 (1997) 1735–1780.

[54] K. Cho, B. Van Merriënboer, C. Gulcehre, D. Bahdanau, F. Bougares, H. Schwenk, Y. Bengio, Learning phrase representations using rnn encoder-decoder for statistical machine translation, arXiv preprint arXiv:1406.1078 (2014).

[55] Y. Xu, X. Lu, Y. Fei, Y. Huang, Iterative self-transfer learning: A general methodology for response time-history prediction based on small dataset, Journal of Computational Design and Engineering 9 (2022) 2089–2102.

[56] Y. Xu, X. Lu, Y. Fei, Y. Huang, Hysteretic behavior simulation based on pyramid neural network: Principle, network architecture, case study and explanation, Advances in Structural Engineering 26 (2023) 2359–2374.

[57] Y. Gu, X. Lu, Y. Xu, A deep ensemble learning-driven method for the intelligent construction of structural hysteresis models, Computers & Structures 286 (2023) 107106.

[58] A. Vaswani, N. Shazeer, N. Parmar, J. Uszkoreit, L. Jones, A. N. Gomez, Ł. Kaiser, I. Polosukhin, Attention is all you need, Advances in neural information processing systems 30 (2017).

[59] N. Kitaev, Ł. Kaiser, A. Levskaya, Reformer: The efficient transformer, arXiv preprint arXiv:2001.04451 (2020).

[60] H. Zhou, S. Zhang, J. Peng, S. Zhang, J. Li, H. Xiong, W. Zhang, Informer: Beyond efficient transformer for long sequence time-series forecasting, in: Proceedings of the AAAI conference on artificial intelligence, volume 35, 2021, pp. 11106–11115.

[61] H. Wu, T. Hu, Y. Liu, H. Zhou, J. Wang, M. Long, Timesnet: Temporal 2d-variation modeling for general time series analysis, in: The eleventh international conference on learning representations, 2022.

[62] D. Shi, Y. Xu, G. Lu, Z. Li, C. Demartino, Glubam roof truss with riveted glubam connections adopting thin-walled steel tube: Experiment, modeling, and model-updating, Journal of Building Engineering 96 (2024) 110550.

[63] W. Stewart, The seismic design of plywood sheathed shear walls, Ph.D. thesis, University of Canterbury, 1987.

[64] B. Folz, A. Filiatrault, Seismic analysis of woodframe structures. i: Model formulation, Journal of Structural Engineering 130 (2004) 1353–1360.

[65] L. N. Lowes, N. Mitra, A. Altoontash, A beam-column joint model for simulating the earthquake response of reinforced concrete frames, peer report, Pacific Earthquake Engineering Research Center, University of California, Berkeley, CA (2003).

[66] H. Dong, M. He, X. Wang, C. Christopoulos, Z. Li, Z. Shu, Development of a uniaxial hysteretic model for dowel-type timber joints in opensees, Construction and Building Materials 288 (2021) 123112.

Appendix A. Introduction of basic material models

(a) Behavior of Tension-STOP (TS_i) material

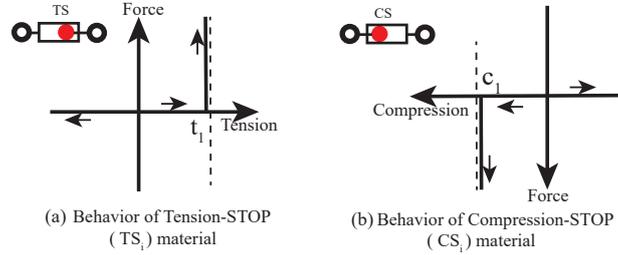(b) Behavior of Compression-STOP (CS_i) material

Figure A.16: Behavior of STOP (S) material model: Tension-STOP (TS) material model (a) and Compression-STOP (CS) material model (b). (modified based on Shi et al. [36, 38])
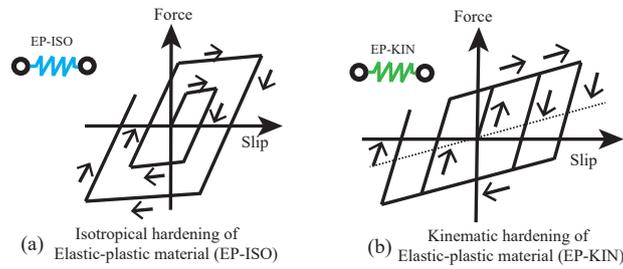

(a) Isotropical hardening of Elastic-plastic material (EP-ISO)

(b) Kinematic hardening of Elastic-plastic material (EP-KIN)

Figure A.17: Behavior of Elasto-plastic (EP) material model: Isotropic hardening Elasto-plastic (EP-ISO) material model (a) and Kinematic hardening Elasto-plastic (EP-KIN) material model (b). (modified based on Shi et al. [36, 38])
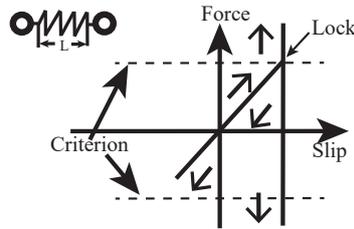

Figure A.18: Behavior of LOCK (L) material model. (modified based on Shi et al. [36, 38])

29

(a) Model of fastener   (b) Monotonic behavior of fastener   (c) Hysteresis behavior of fastener
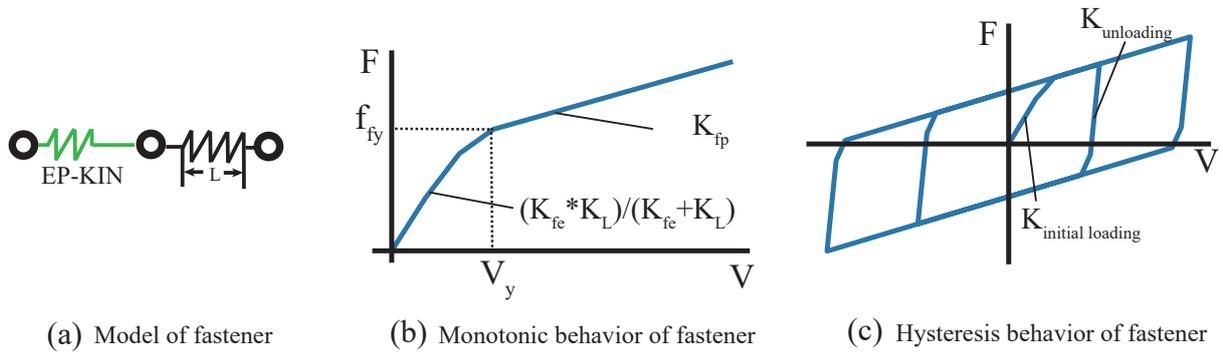
Figure A.19: Constitutive rule of fastener model: configuration of fastener model (a), monotonic behavior of fastener (b) and hysteresis behavior of fastener (c). (modified based on Shi et al. [36, 38])
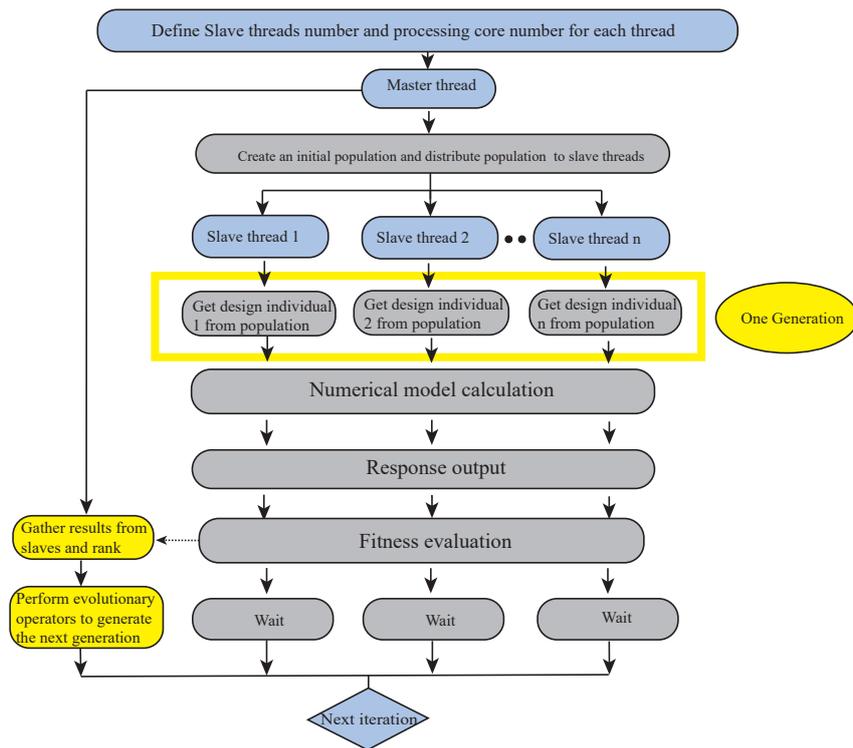
Appendix B. Flowchart for PGA

Figure B.20: Flowchart for parallel algorithm. (modified based on Shi et al. [36])